ARL-TR-10281 ● JAN 2026

2D-Wedge Impact Response of Film-Based UHMWPE Composites as a Function of Loading Rate and Indenter Geometry

by C. Allan Gunnarsson and Tusit Weerasooriya

NOTICES

Disclaimers

ARL-TR-10281 ● JAN 2026

2D-Wedge Impact Response of Film-Based UHMWPE Composites as a Function of Loading Rate and Indenter Geometry

C. Allan Gunnarsson and Tusit Weerasooriya
DEVCOM Army Research Laboratory

REPORT DOCUMENTATION PAGE

1. REPORT DATE	2. REPORT TYPE	3. DATES COVERED START DATE	END DATE
January 2026	Technical Report	1 April 2023	1 August 2025

4. TITLE AND SUBTITLE
2D-Wedge Impact Response of Film-Based UHMWPE Composites as a Function of Loading Rate and Indenter Geometry

5a. CONTRACT NUMBER	5b. GRANT NUMBER	5c. PROGRAM ELEMENT NUMBER
5d. PROJECT NUMBER	**5e. TASK NUMBER**	**5f. WORK UNIT NUMBER**

6. AUTHOR(S)
C. Allan Gunnarsson and Tusit Weerasooriya

7. PERFORMING ORGANIZATION NAME(S) AND ADDRESS(ES)	8. PERFORMING ORGANIZATION REPORT NUMBER
DEVCOM Army Research Laboratory ATTN: FCDD-RLA-TB Aberdeen Proving Ground, MD 21005	ARL-TR-10281

9. SPONSORING/MONITORING AGENCY NAME(S) AND ADDRESS(ES)	10. SPONSOR/MONITOR'S ACRONYM(S)	11. SPONSOR/MONITOR'S REPORT NUMBER(S)

12. DISTRIBUTION/AVAILABILITY STATEMENT
DISTRIBUTION STATEMENT A. Approved for public release: distribution unlimited.

13. SUPPLEMENTARY NOTES
ORCIDs: C. Allan Gunnarsson, 0000-0002-8472-5193; Tusit Weerasooriya, 0000-0003-3299-2166

14. ABSTRACT
An experimental method was developed to obtain the rate-dependent deformation and failure response of ultra-high-molecular-weight polyethylene (UHMWPE) composites during penetration while allowing for strain measurements of the response that are traditionally unavailable during ballistic experiments. The composites were fabricated using solid-state extruded unidirectional films. The loading rate varied from low-rate indentation to high-rate impact using a modified split-Hopkinson pressure bar. Different deformation and failure mechanisms were observed by varying the indenter geometry and specimen boundary conditions. Indenter geometries ranged from blunt (for tension and compression dominated stress state) to ultra-sharp (razor blade) for shear cutting dominated. Boundary conditions included the unbacked configuration, in which the specimen backface was unconstrained, and the backed configuration, where specimen motion was constrained. The experiments enabled measurement of the strain profile ahead of the indenter during loading. The deformation and failure responses were dependent on indenter geometry, with higher sharpness corresponding to lower loads, as well as boundary condition, with the unbacked configuration dominated by bending while the backed configuration was dominated by shear cutting and transverse sliding. These experimental findings address a critical knowledge gap and have been used to develop rate-dependent deformation and failure computational concepts that incorporate mechanism-based multiaxial deformation and observed dominant failure modes.

15. SUBJECT TERMS
UHMWPE, solid-state extrusion, SSE, film composites, high-rate impact loading, split-Hopkinson pressure bar, SHPB, composite shear and cutting failure characterization, digital image correlation, DIC, composite laminate indentation, Terminal Effects

16. SECURITY CLASSIFICATION OF: a. REPORT	b. ABSTRACT	C. THIS PAGE	17. LIMITATION OF ABSTRACT	18. NUMBER OF PAGES
UNCLASSIFIED	UNCLASSIFIED	UNCLASSIFIED	UU	36

19a. NAME OF RESPONSIBLE PERSON	19b. PHONE NUMBER *(Include area code)*
C. Allan Gunnarsson	(520) 691-5721

STANDARD FORM 298 (REV. 5/2020)
Prescribed by ANSI Std. Z39.18

Contents

List of Figures

List of Tables

Acknowledgments

We would like to acknowledge the contributions to this study from Karl Bernetich and Michael Neblett of the ARL Composites and Hybrid Materials Branch for composite plate consolidation and specimen fabrication.

1. Introduction

Traditional ultra-high-molecular-weight polyethylene (UHMWPE) composites have been manufactured by embedding UHMWPE fibers into a softer matrix material, such as Dyneema HB26 that features Dyneema SK76 fibers embedded in a polyurethane matrix (Alexander and Weerasooriya 2021). More recently, UHMWPE composites are being manufactured without the use of fibers by using a process called solid-state extrusion (SSE) to produce films. When compared to fiber-based, SSE film UHMWPE composites cost less to manufacture and may provide equal or improved protection levels (Singletary and Lauke 2016; Cline and Love 2020; Reddy et al. 2020). Tensylon is a commercially available example of an SSE film-based UHMWPE composite.

However, prediction of the deformation and failure response of UHMWPE composites remains a challenge. Creation of computational modeling methods that can predict the deformation and failure of composites based on UHMWPE films and fibers during impact requires mechanistic understanding of deformation and failure response of the subscale constituent materials and mesoscale understanding of shear and tensile delamination of plies.

Implementation of rate-dependent subscale mechanistic failure concepts to predict failure during penetration requires rate-dependent failure thresholds for each dominant failure mechanism, assuming the complex coupling between mechanisms as a second-order effect. For implementation of the mesoscale delamination process in modeling, rate-dependent mixed-mode traction separation laws (TSLs) are needed. Obtaining Mode 1 (tensile) and Mode 2 (shear) TSLs allows implementation of methods to incorporate the delamination failure process during impact and penetration into layered composites. Mode 2 (shear) TSLs were developed for fiber-based (Alexander et al. 2023) and film-based (Alexander and Weerasooriya 2024) UHMWPE layered composites; development of Mode 1 (tensile) TSLs for UHMWPE layered composites is currently ongoing.

To address this challenge, a series of experiments have been developed. At the subscale, the tensile properties of UHMWPE single fibers and films loaded in a uniaxial stress state were investigated. Sanborn et al. (2015) characterized the failure strengths of single SK76 UHMWPE fibers as a function of loading rate. Thomas et al. (2018) characterized the tensile strength of single SK76 UHMWPE fibers that had been damaged previously by transverse compression. Gunnarsson et al. (2022) characterized the tensile behavior of unidirectional (UD) SSE UHMWPE (Tensylon) films as a function of strain rate. The effect of indenter geometry (blunt to razor) during transverse loading on UHMWPE single fiber failure was studied at high loading rates by Thomas et al. (2021).

To understand how UHMWPE composites delaminate (Mode 2 shear) between UD layers, direct and indirect methods have been developed. Shear delamination of UHMWPE has been studied (Meshi et al. 2016; Bogetti et al. 2017) at low loading rate. Thomas et al. (2025) directly characterized the interlaminar Mode 2 shear response of Tensylon SSE film at high loading rate by using cross-ply specimens with a small UD layer count and introducing a pre-crack in the specimens to preferentially induce pure shear between the UD layers. Gunnarsson et al. (2023) compressed cross-ply film- and fiber-based UHMWPE composites at an offset angle relative to the axis of the UD layers. The measured response of these low-angle (15°) offset-shear experiments was dominated by interlaminar shear, such that the interlaminar shear properties were able to be inferred through inverse simulation and were used to develop rate-dependent Mode-2 shear cohesive laws that govern shear delamination failure for film-based (Alexander et al. 2023) and fiber-based (Alexander and Weerasooriya 2024) UHMWPE composites. The in-plane compressive behavior of cross-ply UHMWPE composites has been studied as a function of loading rate (Liu et al. 2019), which resulted in ply buckling and separation.

It is necessary, however, to move from the uniaxial stress state induced in subscale experiments to the multiaxial stress state induced during impact. Characterization of the multiaxial response is key for the development of physics-based methods for computational prediction of the deformation and failure of UHMWPE composites, such as the concepts formulated by Alexander et al. (2023). Implementation of these rate-dependent subscale mechanistic failure concepts to predict failure during penetration requires rate-dependent failure thresholds for each dominant failure mechanism. The experimental techniques developed here allow for an inverse method using critical experiments with computational modeling to obtain those thresholds.

Here, a novel 2D wedge-indent experimental method was developed to obtain the deformation and failure response of UHMWPE composites as a function of loading rate from low to high rate, and as a function of indenter geometry while measuring specimen full-field strain ahead of the indenter. Varying the indenter geometry imparted different multiaxial stress states on the composite. Thin-beam SSE film-based UHMWPE laminated composite specimens with a known number of UD layers were loaded using indenters with geometry varying from ultra-sharp (razor blade) to blunt (half-cylinder), at low (0.005 mm/s) and high (5 m/s, modified split-Hopkinson pressure bar [SHPB]) loading rates. These indenter geometries provide stress states at the target interaction zone (TIZ) ranging from shear cutting dominated to tensile deformation dominated. This experimental method was applied to laminated SSE film-based UHMWPE composites (Tensylon HSBD-30A). This experimental technique provided measurement of deformation in the TIZ during loading; this allowed for the quantification of strain fields during loading and failure in the TIZ. In this report, the experimental techniques and results are reported. This experimental research addresses a critical knowledge gap and is being used to develop rate-dependent inverse computational concepts incorporating mechanism-based multiaxial failure models. These results are being used to develop customized components for computer codes to accurately predict the impact response of laminated composites.

2. Methods

2.1 Materials

The material used in this study was supplied in the form of precursor sheets, wound into large rolls. Each precursor sheet comprised two UD layers bonded together in a cross-ply (0/90) configuration. Tensylon HSBD-30A (manufactured by DuPont and referred to here as Tensylon 30A) was used for the UHMWPE composite and is based on a solid-state extruded film/tape at the UD layer length scale.

2.2 Specimen Fabrication

Thin beam specimens were extracted from a Tensylon 30A panel (12 × 12 inches) that was consolidated following manufacturer's recommendations in a confined mold. It was heated at 175 °F, 870 psi for 10 min, and at 230 °F, 2000 psi for 20 min. The panel was consolidated using 24 precursor sheets, corresponding to 48 UD layers. After consolidation, the Tensylon 30A panel had an average thickness of 2.79 mm, with a consolidated UD layer thickness of 58.1 µm. The consolidated composite panel was waterjet cut to create beam specimens with the plate thickness. The nominal width (y-dimension, Figure 1) was 4 mm for most specimens, although for several experiments, a different width was used; these are discussed later (Section 3.1.2). The waterjet cutting process created slight raised edges on the specimens; the specimens were lightly wet sanded to remove the edges and ensure the specimen surfaces were flat and parallel. Figure 1 shows the consolidated Tensylon 30A panel and thin beam specimens extracted via waterjet.

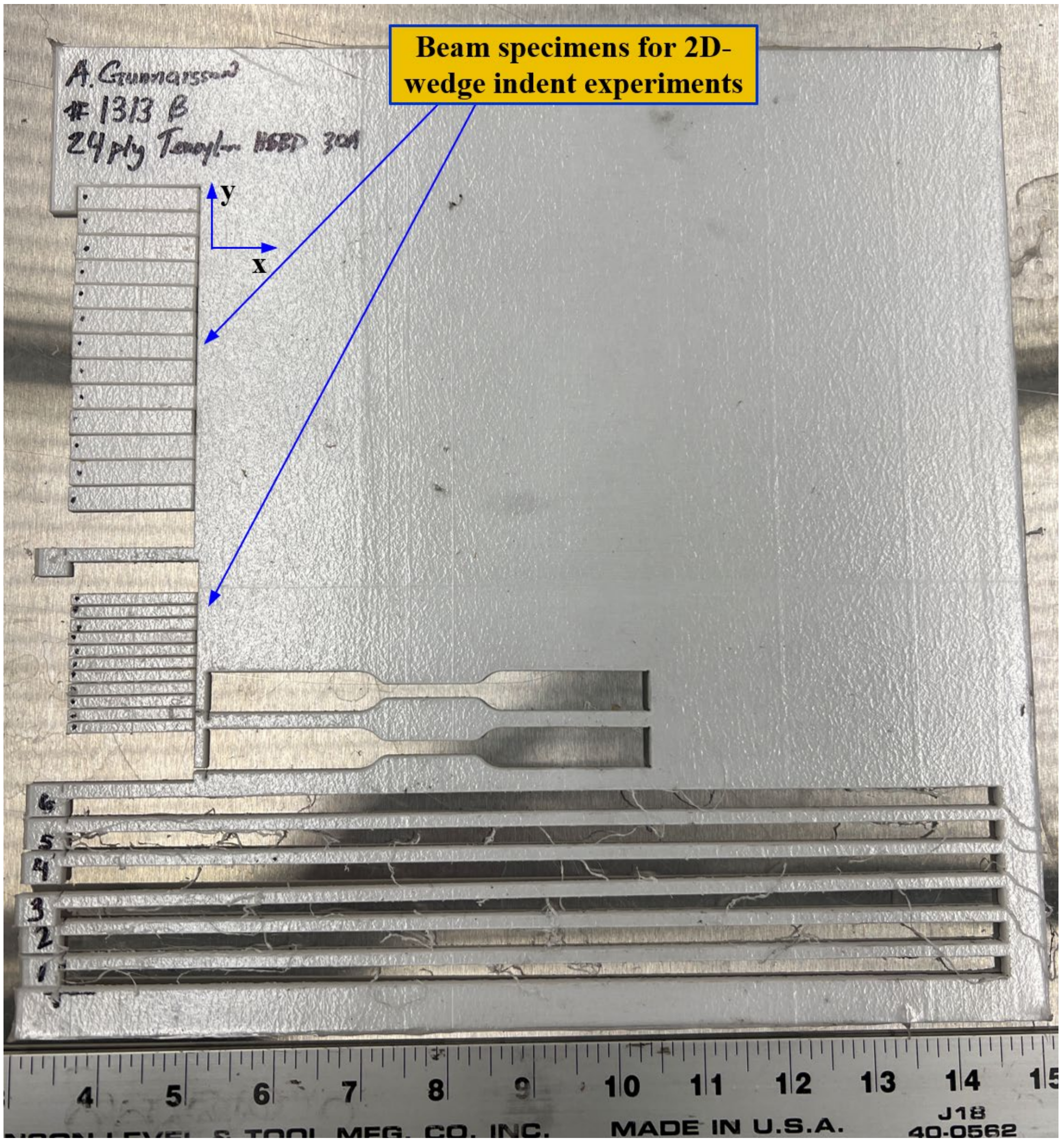

Figure 1. Consolidated Tensylon 30A panel showing beam specimen extraction by micro waterjet cutting. Scale marked in inches. (Tension [dogbone] specimens shown extracted in the photo are not documented here.)

2.3 Experiments

The laminate beam specimens were loaded by indenters with different tip geometries. The different indenter geometries were used to create different stress states within the specimen during loading and different failure modes. Two different backing configurations were used. The first configuration, referred to as "backed configuration," had the specimens constrained on the opposite surface from the indenter. The second configuration, referred to as "unbacked configuration," had the specimens unconstrained on the opposite surface from the indenter, somewhat similar to a three-point bending experiment. A schematic of the backed loading configuration is shown in Figure 2, and the unbacked loading configuration is shown in Figure 3, both for high loading rate. The unbacked configuration was loaded with a specimen adapter that was designed for the specimen ends to rest on rounded supports with a radius (Figure 3) of 6.35 mm (0.25 inches) while the specimen center region (including the TIZ), with a span (Figure 3) of 14.3 mm (0.5625 inches) was free to deform. The specimen ply layup direction is indicated in the two schematics by arrows.

Figures 2 and 3 show schematics for the high loading rate; the low loading rate configuration is similar, while using a hydraulic test machine for indenter displacement. At low rate, the indenter is attached to a load cell and hydraulic test machine actuator for indenter displacement and load measurement. For the backed configuration, the specimen rests on a compression platen, while for the unbacked configuration, the specimen sits on the unbacked adapter mounted to a compression platen.

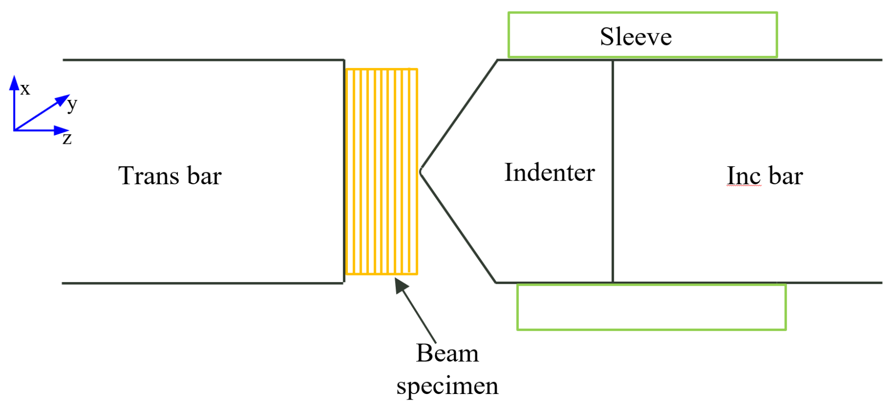

Figure 2. Laminate indent loading experiment and specimen orientation schematic for backed configuration at high loading rate. Trans and Inc bars refer to the transmission and incident bars of the SHPB setup, as described in Section 2.3.2.

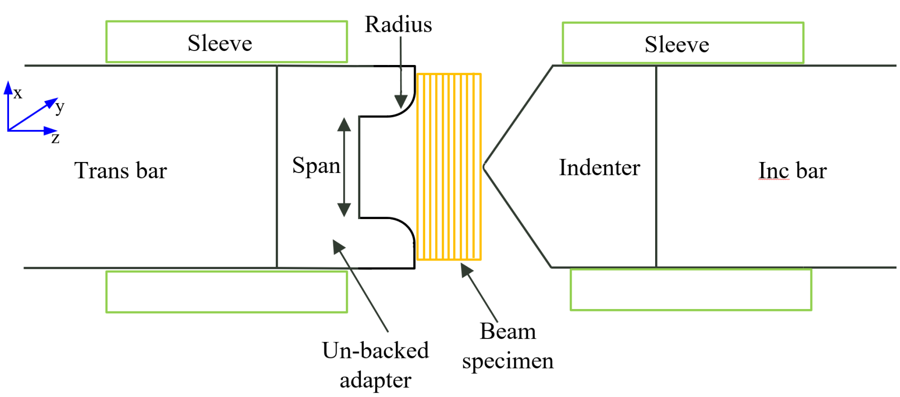

Figure 3. Laminate indent loading experiment and specimen orientation schematic for unbacked configuration at high loading rate. Trans and Inc bars refer to the transmission and incident bars of the SHPB setup, as described in Section 2.3.2.

For all experiments, 2D digital image correlation (DIC) was performed to quantify specimen deformation and failure during loading in the TIZ. The beam specimens were speckled using a flat white spray-paint base coat and a black spray-paint speckle layer over the base layer. Postprocessing of images was performed using commercially available software (Correlated Solutions Vic2D). For all strain analysis, the engineering strain tensor was used. The different indenter geometries are referred to as blunt, intermediate, sharp, and razor (or ultra-sharp). The tip radius at specimen contact is varied for each; they are 15.875 mm (0.625 inches) for blunt, 0.381 mm (0.015 inches) for intermediate, 0.0254 mm (0.001 inches) for sharp, and 0.005 mm (0.0002 inches) for razor, achieved using a razor blade as the indenter. For the razor, the blade taper angle was measured to be about 15°. For both sharp and intermediate indenters, the wedge angle was 40°. Figure 4 shows examples of the four different indenters, while Figure 5 shows typical microscopy of the indenter tips.

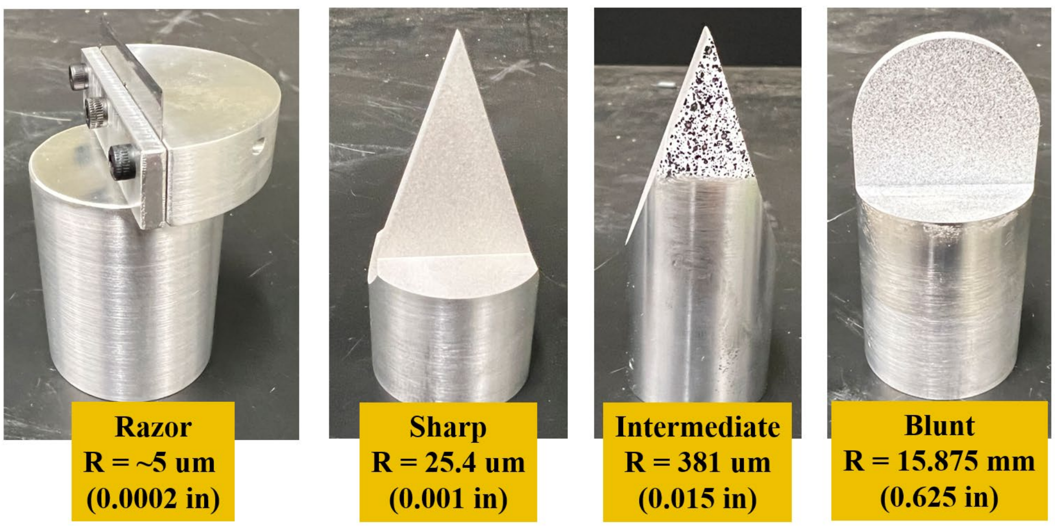

Figure 4. Indenter geometries for blunt, intermediate, sharp, and razor indenters.

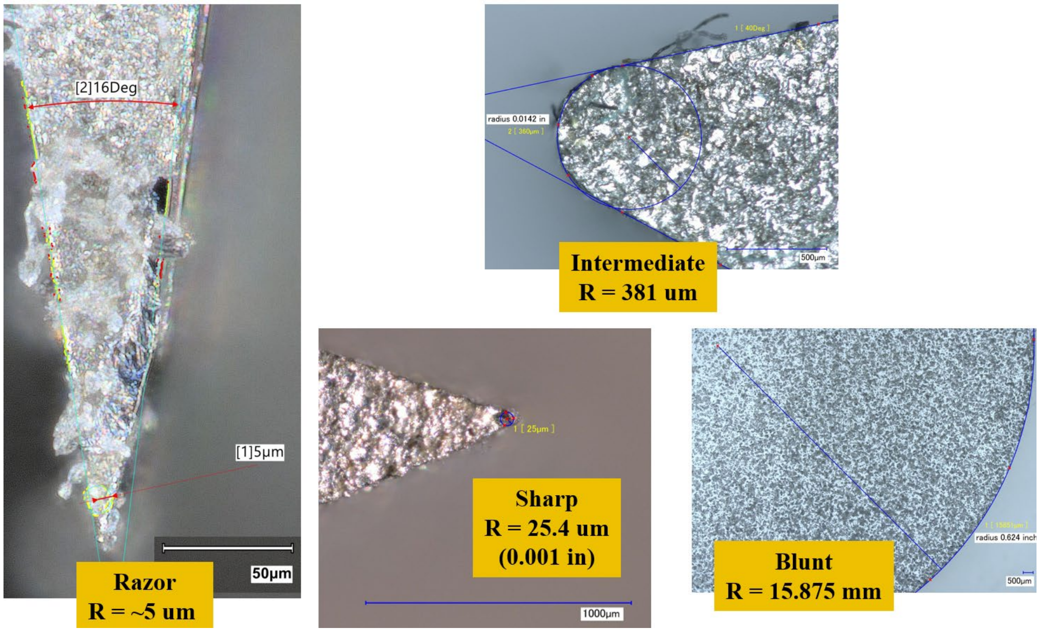

Figure 5. Indenter microscopy for blunt, intermediate, sharp, and razor indenters.

2.3.1 Low Loading Rate Experiments

For the low loading rate experiments, a servo-hydraulic Instron test frame (Figure 6, shown with blunt geometry indenter) was used to apply indent loading on the beam specimens at a constant velocity of 0.005 mm/s. At the low loading rate, a framing camera captured the specimen during loading (FLIR 12.3-megapixel camera at 2 fps).

Figure 6. Loading setup for low loading rate experiments, pictured with blunt geometry indenter.

2.3.2 High Loading Rate Experiments

High loading rate indent experiments were performed on beam specimens using a modified version of a typical compressive SHPB setup with the following details. The operation and theory of the SHPB are omitted for brevity, as extensive literature on this topic does exist (Schreier et al. 2009; Chen and Song 2010). The SHPB setup consisted of Al 7075 alloy 31.8-mm-diameter (1.25-inch) incident bar, transmission bar, and striker of lengths 3.66 m (144 inches), 2.44 m (96 inches), and 0.61 m (24 inches), respectively. The unbacked adapter was also fabricated from Al 7075. The indenters were attached to the incident bar using a nylon sleeve, as was the unbacked adapter onto the transmission bar (see Figures 2 and 3). Both semiconductor and traditional resistive gages were used on the incident and transmission bars; semiconductor gages are known to be highly sensitive to environmental conditions and were calibrated with the stable resistive gages. Figure 7 shows the aluminum SHPB used for laminate indent experiments with intermediate geometry indenter. For all high-rate experiments, wave shaping was employed to reduce dispersive effects resulting in increased pulse rise time.

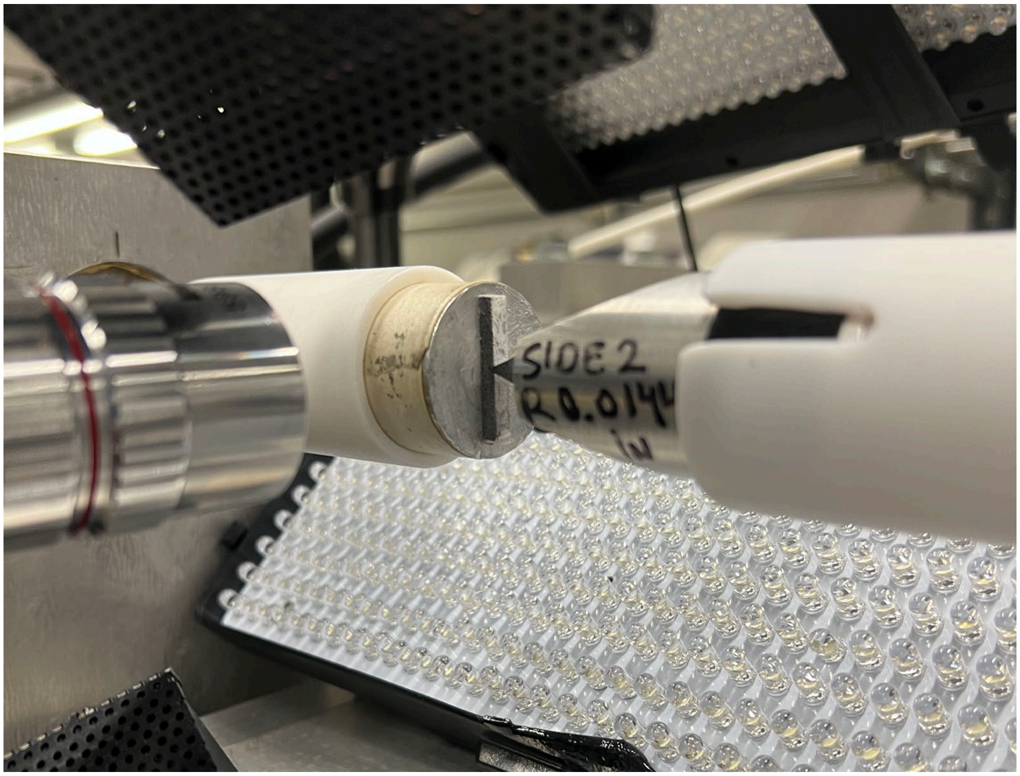

Figure 7. Loading setup for high loading rate experiments. Pictured is the intermediate geometry indenter in backed configuration from experiment T35.

Two high-speed cameras were used to image the high loading rate experiments. A Shimadzu HPV-2 ultra-high-speed camera was used at 125,000 fps to image the specimen during loading. These images were postprocessed to obtain specimen deformation using DIC software (Correlated Solutions VIC-2D). Results from this camera are referred to as loading point images, as this camera's field of view was focused on the specimen at the loading point where the indenter contacts the specimen. High-intensity LED lights were used to illuminate the specimen during loading; to avoid any heating of the specimen, these lights were turned on just prior to loading. In addition, a Photron Nova S16 ultra-high-speed camera was used at 200,000 fps to image both the indenter and transmission bar during loading. These images allowed for postprocessing to obtain displacements of both the indenter and the transmission bar using the same DIC software. Results from the camera are referred to as whole specimen images, as this camera had a field of view capturing the whole specimen as well as portions of the transmission bar and indenter. Figure 8 shows typical images from a high loading rate indent experiment from the loading point camera (Figure 8a) and whole specimen camera (Figure 8b); these cameras are imaging opposite sides of the specimen. The images in Figure 8 are from indent experiments with backed configuration and intermediate geometry indenter.

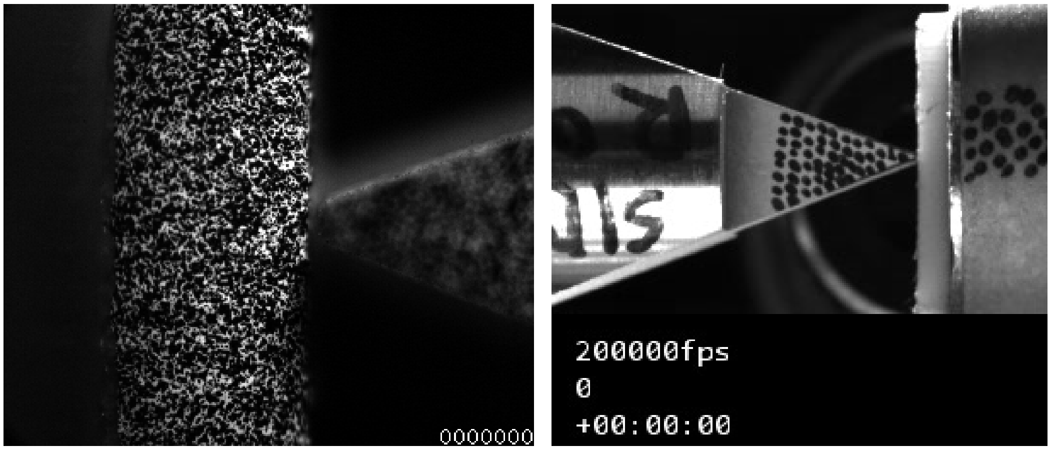

(a) (b)

Figure 8. Tensylon 30A laminate indent with intermediate geometry indenter at high loading rate in backed configuration experiment initial images at 0 μs (just before loading) from (a) loading point camera and (b) whole specimen camera. Note that the two cameras are imaging opposite sides of the specimen.

3. Results

The following sections of this report summarize the experimental data and results from the laminate indent experiments for Tensylon 30A. Table 1 summarizes the experiments performed and results for Tensylon 30A. The various measurements recorded in the tables are described herein. Specimen dimensions are referred to as thickness, width, and length; these correspond to the specimen measurements along the *z*-axis (loading axis), *y*-axis, and *x*-axis, respectively, in the loading schematics in Figures 2 and 3 from Section 2.3.

Table 1. Summary of experimental results for Tensylon 30A laminate indent loading experiments.

Configuration	Loading rate	Indenter	Thickness (mm)	Width (mm)	Length (mm)	Indenter disp. rate (mm/s)	Loading rate (kN/s)	Initial stiffness (kN/mm)	Failure load (kN)[c]
Backed	High	Blunt	2.89	4.42	25.4	3570	11334	41.50[a]	13.3
		Inter	2.93	4.54	26.6	4170	9564.4	3.09	1.09
		Sharp	2.86	4.34	25.8	4242	3783.8	1.01	0.507
		Razor	2.93	4.37	39.1	4789	3311.5	0.68	0.205
	Low	Blunt	2.86	4.39	51.2	0.0508	1.30	47.30[a]	11.44[b]
		Inter	2.85	7.79	38.1	0.0508	0.504	9.94	7.7
		Sharp	2.97	4.52	25.1	0.0505	0.153	3.01	. . .
		Razor	2.89	4.38	20.9	0.0507	0.044	0.89	0.214
Unbacked	High	Blunt	2.93	4.38	37.2	4573	242.8	0.082	. . .
		Inter	2.97	4.53	38.3	5123.7	1002.0	0.196	. . .
		Sharp	2.95	4.38	32.4	4877.9	504.8	0.089	. . .
		Razor	2.95	4.47	76.1	4623.5	293.9	0.057	. . .
	Low	Blunt	2.93	3.70	38.1	0.0506	0.0053	0.104	. . .
		Inter	2.79	4.29	63.5	0.0507	0.00472	0.091	. . .
		Sharp	2.83	4.32	38.8	0.0508	0.00551	0.113	. . .
		Razor	2.93	4.34	35.8	0.0508	0.00617	0.121	. . .

[a] Initial stiffness for both backed configuration blunt experiments was obtained using a linear fit over the loading range corresponding to 5.0–12.5 kN.

[b] Failure load for the backed configuration blunt experiment was obtained by visual inspection of experiment images.

[c] Failure load refers to the load at which observable failure began to occur in the specimen, via the dominant failure mode for that loading configuration (cutting, transverse sliding, etc.).

At the low loading rate, the indenter displacement, velocity, and far-field global specimen load were measured using machine load cell and displacement data. At the high loading rate, the indenter displacement and velocity were calculated using DIC on the indenter and transmission bar. Specimen load was calculated using traditional SHPB strain gage analysis obtained from the transmission bar. Specimen load was normalized to specimen width (measured prior to loading). Indenter displacement was normalized using nominal specimen thickness; all specimen dimensions were determined using digital calipers.

Figures 9a and 9b provide an example of the data collected and the normalization process for one representative high loading rate experiment with intermediate geometry indenter specimen in the backed configuration. Figure 9a shows the data prior to normalization for specimen load, indenter displacement, and transmission bar displacement data during loading. Figure 9b shows the normalized load and normalized indenter displacement for the same experiment. The normalized indenter displacement was calculated by subtracting transmission bar displacement from indenter displacement and zeroed at the load onset time. A slight (paper-thin) gap between indenter and specimen was used to ensure there was no preload on the specimen, causing the indenter displacement to increase prior to loading.

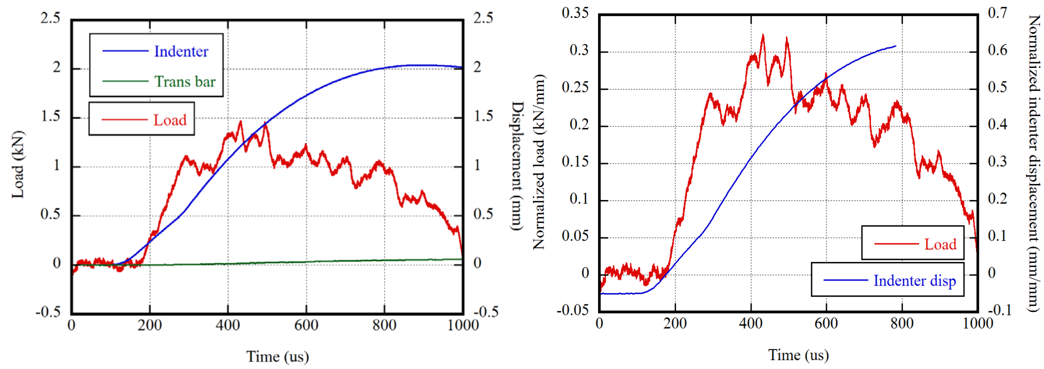

(a) (b)

Figure 9. For high loading rate laminate indent experiment with intermediate geometry indenter in backed configuration, (a) load and displacements for indenter and transmission bar as a function of time during loading and (b) normalized load and indenter displacement as a function of time during loading.

Figure 10 shows the initial (Figure 10a) and final (Figure 10b) images from the loading point camera of a representative high loading rate experiment with sharp geometry indenter in the backed configuration. The image labels denote image time in microseconds, with the final image occurring 404 μs after the initial image.

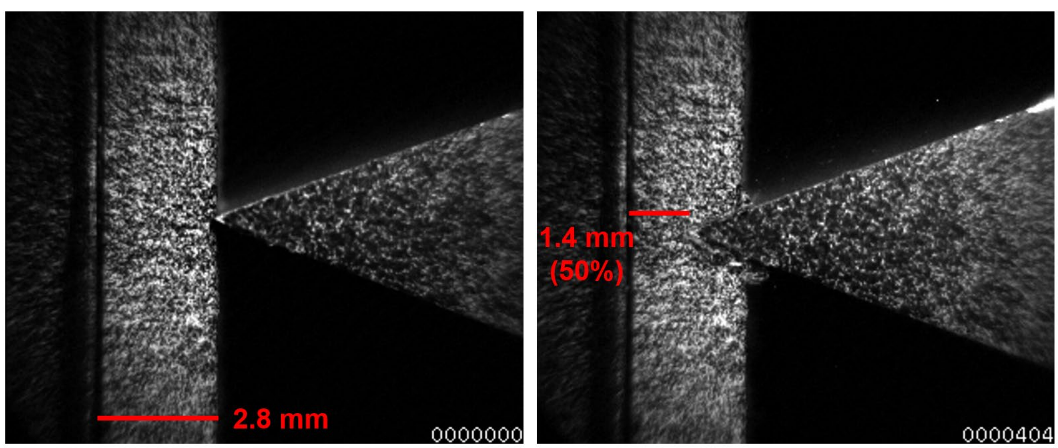

(a) (b)

Figure 10. Images obtained from loading point camera of Tensylon 30A laminate indent experiment with sharp geometry indenter at high loading rate in backed configuration experiment (a) initial image at 0 μs (prior to loading) and (b) final image at 404 μs.

Figure 11a shows the normalized load as a function of normalized indenter displacement for a high loading rate experiment with intermediate geometry indenter in the backed configuration. Figure 11b shows full-field strain profiles at discrete times during loading. The load-displacement graph time labels correspond to the time numbers in the lower-right corner of the strain profile images. These data and corresponding strain profiles were obtained for all experiments documented here; however, for brevity they are omitted.

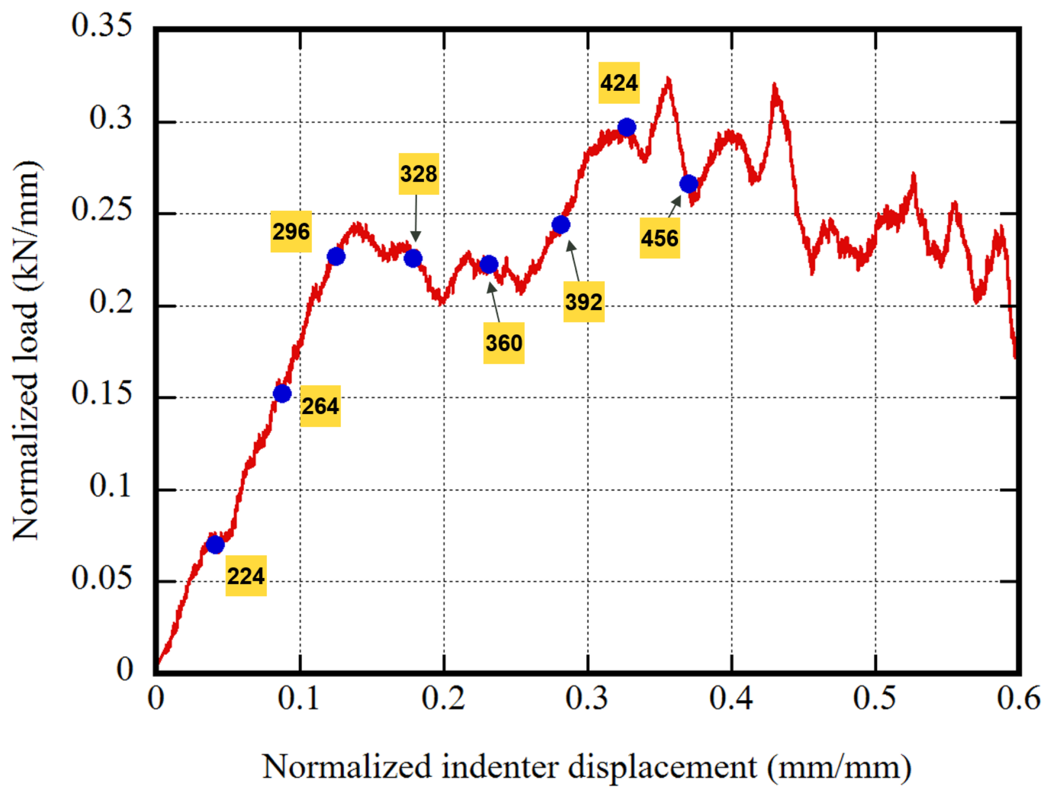

(a)

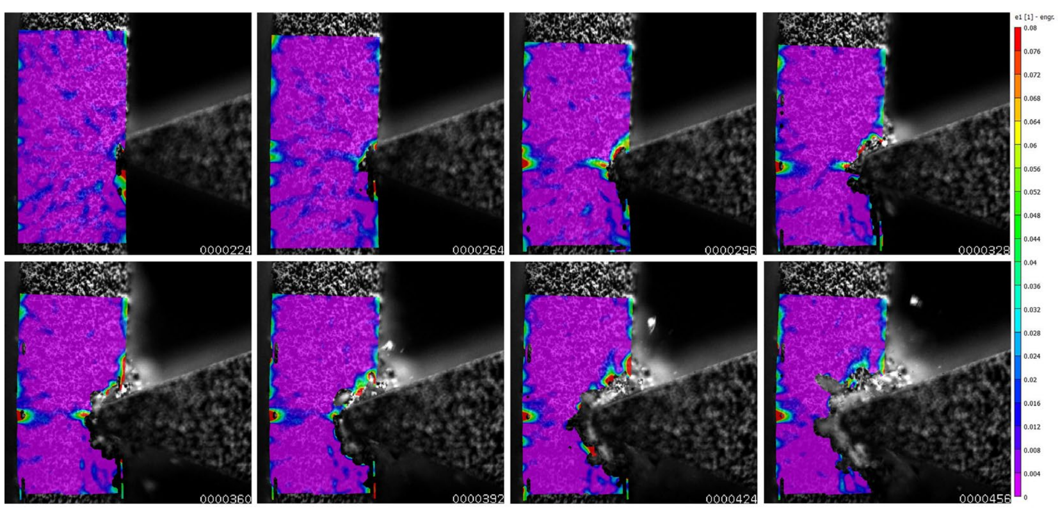

(b)

Figure 11. (a) Normalized load as a function of normalized indenter displacement for a high loading rate experiment with intermediate geometry indenter in the backed configuration (top) and (b) full-field strain profiles at discrete times during loading. The load-displacement graph time labels correspond to the time numbers in the lower-right corner of the strain profile images.

3.1 Backed Configuration Experiments

3.1.1 Effect of Indenter Geometry at Constant Loading Rate

Reported in this section are the normalized load versus normalized corrected indenter displacement data for each of the different indenter geometries for the laminate indent experiments in the backed configuration. To obtain normalized data, the original load and corrected indenter displacement data are divided by the specimen width and thickness, respectively, thus allowing specimens with different dimensions to be compared directly. Figure 12 presents these data for the high loading rate and Figure 13 presents these data for the low loading rate. At high rate, there is a geometry effect, where blunter geometry results in higher loads; this is due to increased indenter tip radius loading a larger specimen area. As the indenter geometry becomes sharper, the specimen area loaded decreases, and failure behavior changes. Failure behavior of the material as a function of indenter geometry is discussed later (Section 3.1.2).

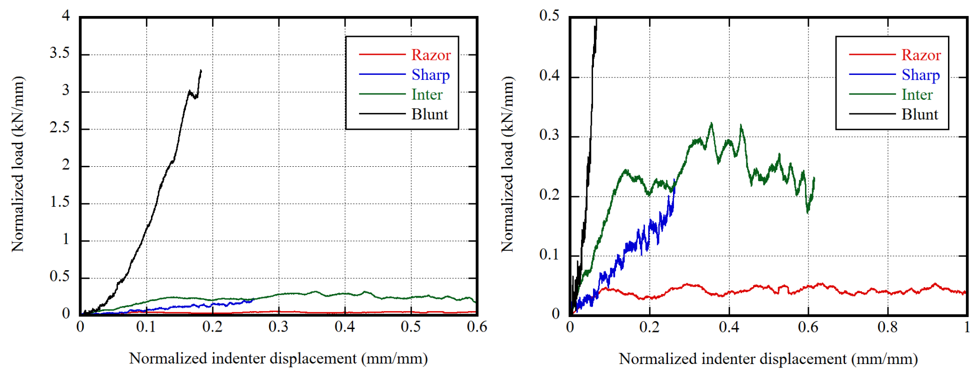

(a) (b)

Figure 12. Normalized load vs. indenter displacement for Tensylon 30A laminate impact experiments in the backed configuration at high loading rate (a) full scale and (b) zoomed in.

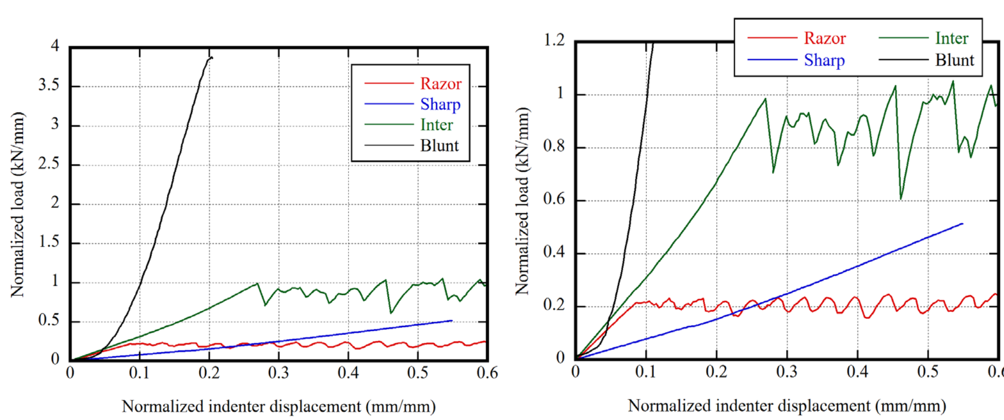

(a) (b)

Figure 13. Normalized load vs. indenter displacement for Tensylon 30A laminate impact experiments in the backed configuration at low loading rate (a) full scale and (b) zoomed in.

3.1.2 Effect of Loading Rate at Constant Indenter Geometry

Reported in this section are the normalized load versus normalized corrected indenter displacement data for both loading rates (low and high rate) with constant indenter geometry for the backed configuration, illustrating the effect of loading rate. Figures 14a, 14b, 14c, and 14d present these data for the blunt, intermediate, sharp, and razor indenter geometries, respectively.

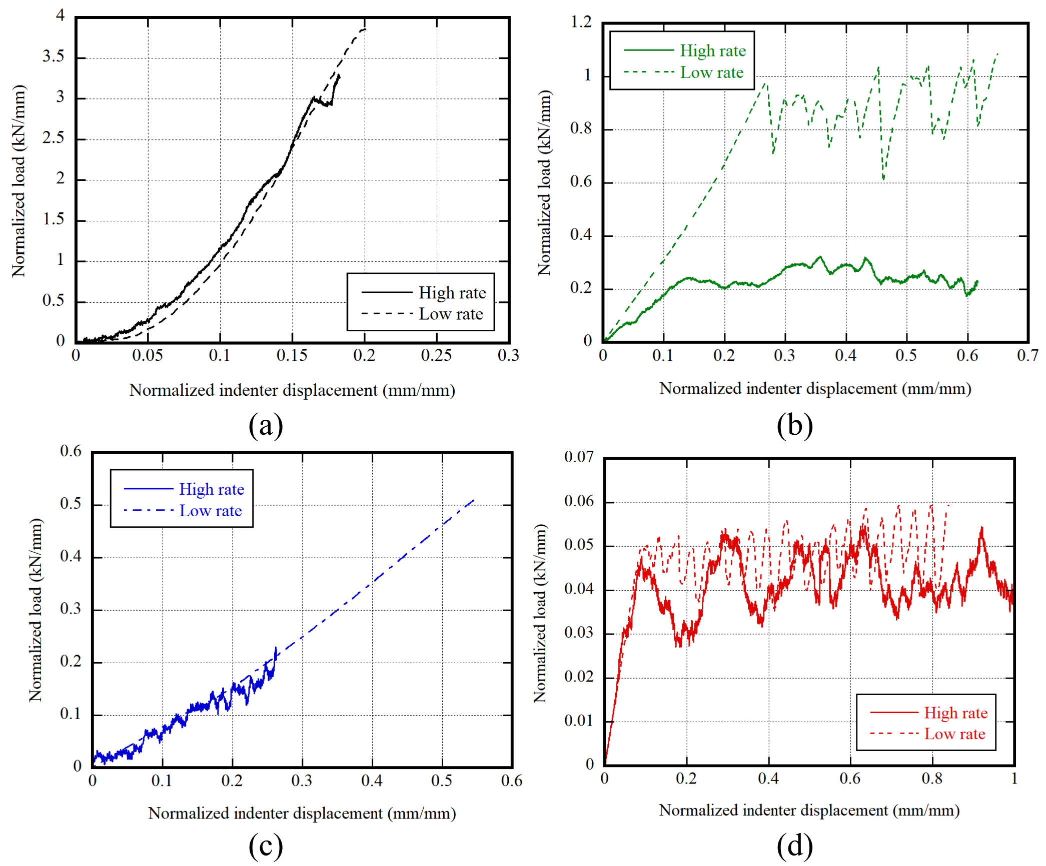

Figure 14. Normalized load vs. normalized corrected indenter displacement data for the backed configuration at both loading rates for constant indenter geometry illustrating the loading rate effect for blunt (a), intermediate (b), sharp (c), and razor (d) indenter geometries.

For the blunt geometry indenter, the mechanical response was almost identical. For both rates, load increased linearly until reaching a point where film layers began sliding transversely.

For the razor indenter, the load increased linearly, until a threshold is reached and the razor starts cutting the laminate layers, leading to a load plateau. Oscillation of the load response in this plateau region is likely due to layer cutting, then slight relaxation, followed by stiffening as the next layer or layer group is engaged until that layer or layer group is cut, followed by slight relaxation, and the cycle repeating. There is a slight trend to increased load during the plateau region, which may correspond to slight dulling of the razor. The response to the razor indenter was rate insensitive, with both low and high loading rates having the same initial stiffness and cutting threshold load.

For the sharp indenter, the mechanical response was almost the same for both rates, with load increasing linearly. No differences in specimen deformation or failure response were observed; at both rates, the specimens deformed with layer delamination and pile-up adjacent to the indenter.

For the intermediate geometry indenter, the mechanical response at the high rate is much lower. This is possibly due to differing failure mechanisms dominating during penetration. At high rate, layer cutting is observed to be the dominant mechanism, with load increasing linearly until layer cutting initiates followed by load plateau, similar to the razor indenter response. At low rate, layer cutting and transverse layer sliding failure mechanisms dominate, with increased load. The low-rate specimen (T39) experienced plastic (permanent) bending deformation that was observable after the end of the experiment, as shown in Figure 15 (bottom left). Bending was observed in the high-rate specimen (T35) during loading using DIC; however, that bending deformation was not plastic—it was recovered after unloading and the specimen returned to flat (Figure 15, bottom right).

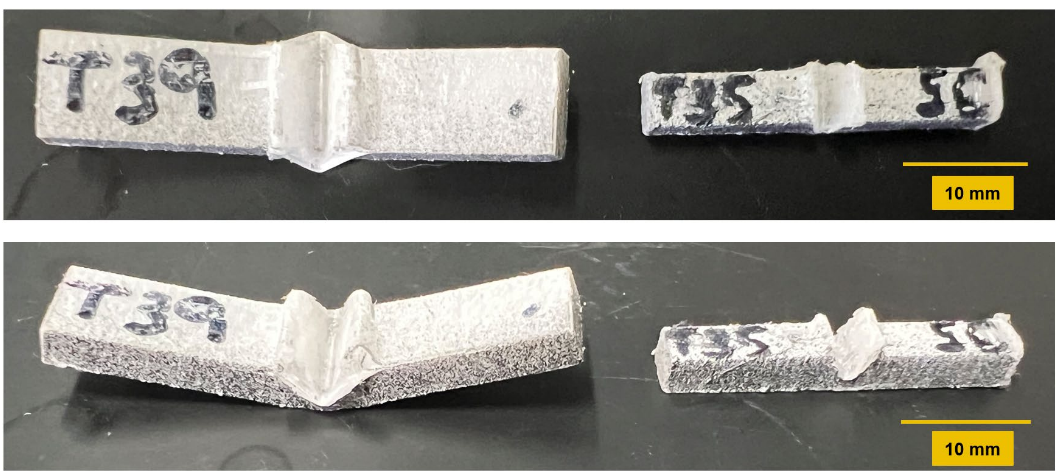

Figure 15. Post experiment photographs of laminate impact experiment specimens for backed configuration with intermediate geometry indenter at low loading rate (left, T39) and high loading rate (right, T35) from a "top view" (top) and a "front view" (bottom).

3.2 Unbacked Configuration Experiments

3.2.1 Effect of Indenter Geometry at Constant Loading Rate

Reported in this section are the normalized load versus normalized corrected indenter displacement data for each indenter geometry for the unbacked configuration laminate impact experiments. Figure 16a presents these data for the high loading rate and Figure 16b presents these data for the low loading rate. The units for these figures have changed to N/mm for normalized load (from kN/mm for the backed configuration results figures in Section 3.1), due to the reduced load capacity of the specimens loaded in the unbacked configuration.

At high rate, there is little geometry effect, with similar load response for all four indenter geometries. In the unbacked configuration, the specimen experiences bending, and it appears that the indenter geometry does not affect the load response. For the low loading rate, there is a small indenter geometry effect, with blunter geometry resulting in larger mechanical response at a later stage of loading after the specimens have started bending.

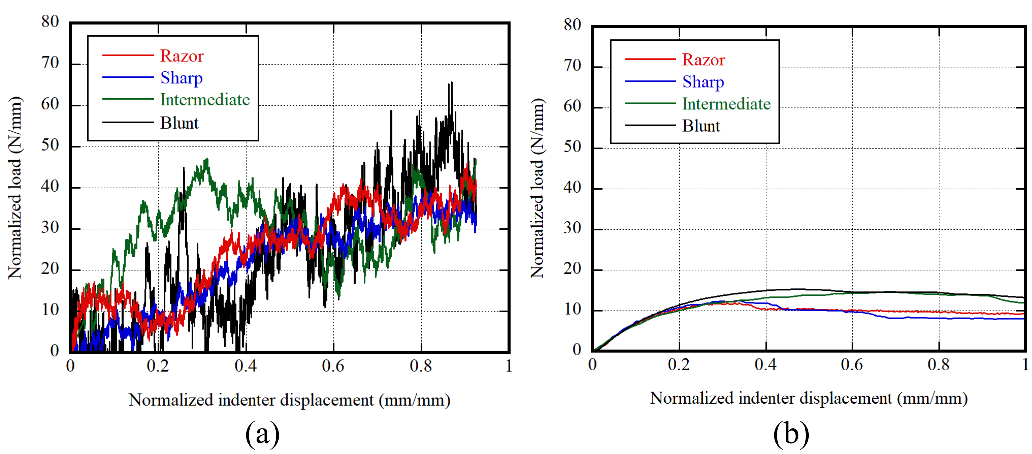

Figure 16. Normalized load vs. indenter displacement for Tensylon 30A laminate impact experiments in the unbacked configuration at (a) high loading rate and (b) low loading rate.

3.2.2 Effect of Loading Rate at Constant Indenter Geometry

Reported in this section are the normalized load versus normalized indenter displacement data for each loading rate with constant indenter geometry for the unbacked configuration, thus illustrating the loading rate effect. Figures 17a, 17b, 17c, and 17d present these data for the blunt, intermediate, sharp, and razor indenter geometries, respectively. For all indenter shapes, higher load was observed for the same indenter displacement, for high loading rate experiments compared to low loading rate experiments.

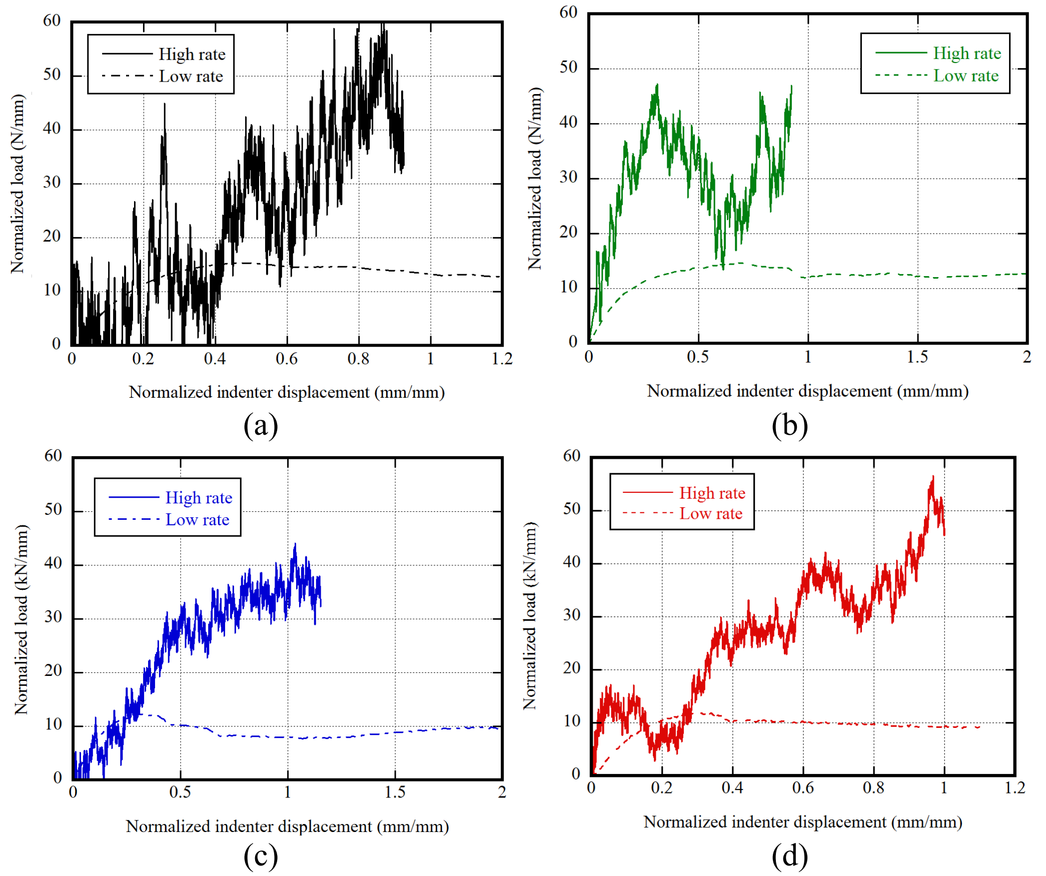

Figure 17. Normalized load vs. normalized corrected indenter displacement data for the unbacked configuration at both loading rates for constant indenter geometry illustrating the loading rate effect for (a) blunt, (b) intermediate, (c) sharp, and (d) razor indenter geometries.

3.3 Laminate Indent Failure Behavior

Different failure behaviors occurred as a result of loading of the laminate indent specimens. These included transverse sliding, pile-up, cutting, different degrees of delamination, and bending. Examples of these are shown in Figures 18–22, which are microscopy images of specimens taken post experiment. These are representative examples to illustrate the behavior referenced in this report; in Figures 18–22, the indenter would be moving downward in the images into the laminate specimens. The observed deformation or failure behavior for each experiment is tabulated in Table 2.

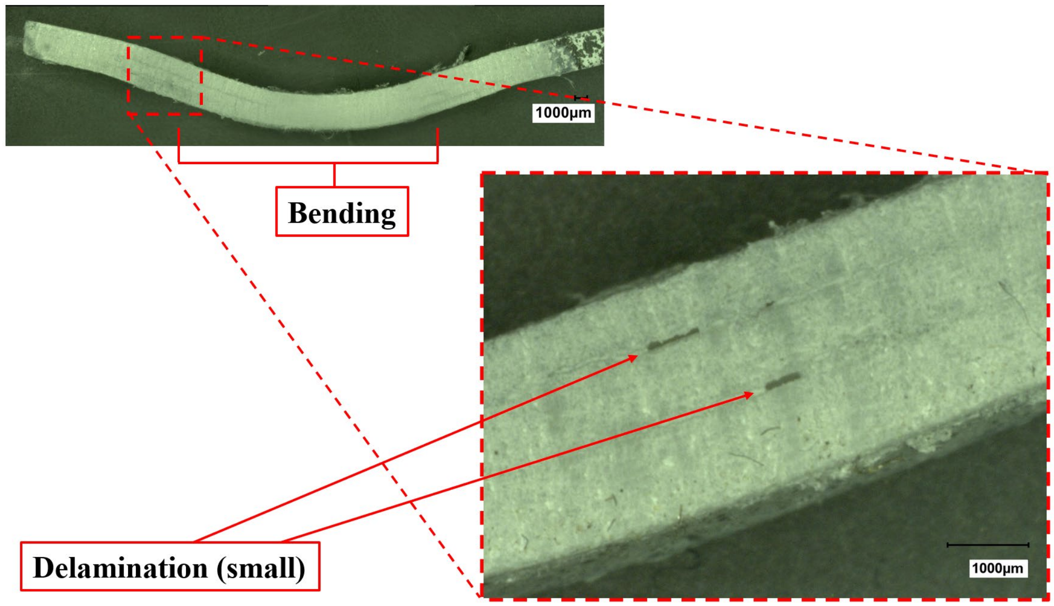

Figure 18. Example of small delamination, bending from high-rate indent experiment with blunt indenter in unbacked configuration.

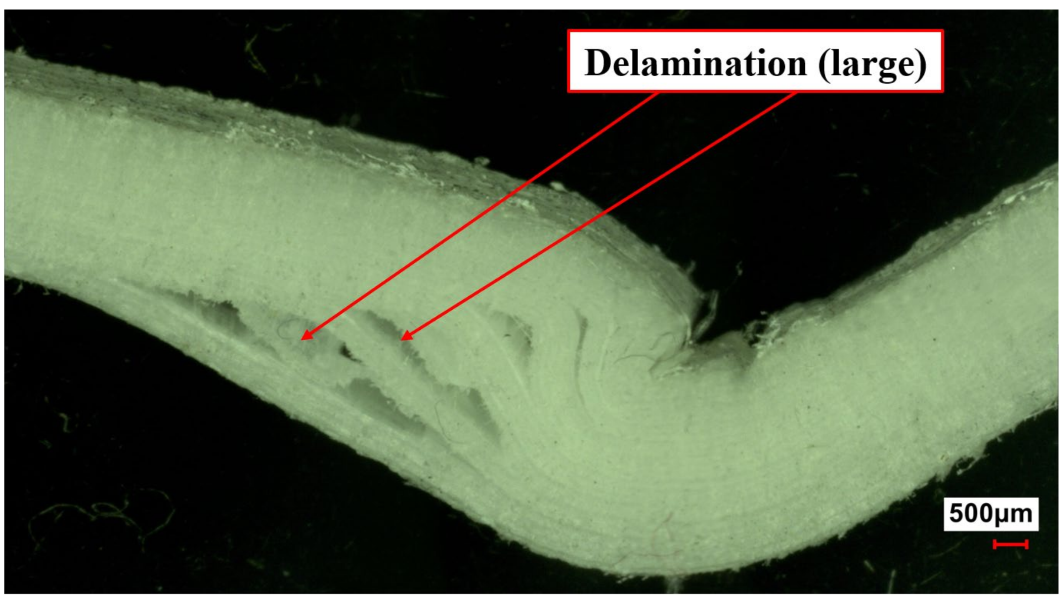

Figure 19. Example of large delamination from high-rate indent experiment with sharp indenter in unbacked configuration.

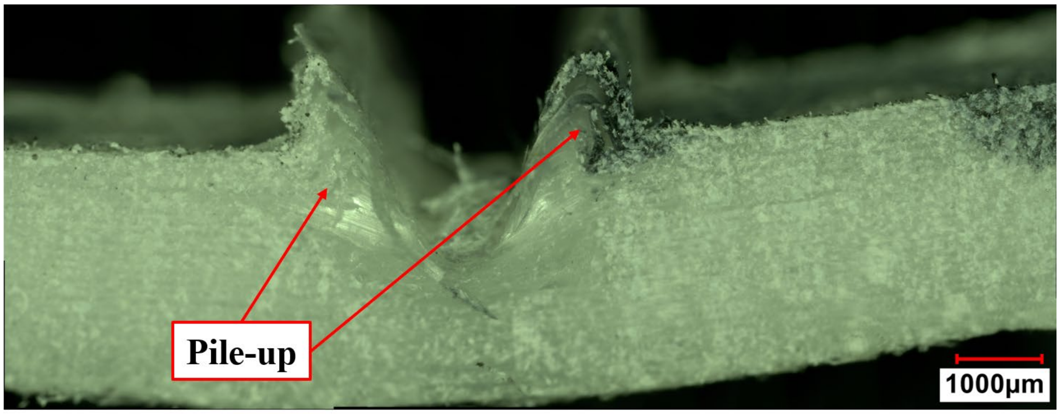

Figure 20. Example of pile-up from high-rate indent experiment with intermediate indenter in backed configuration.

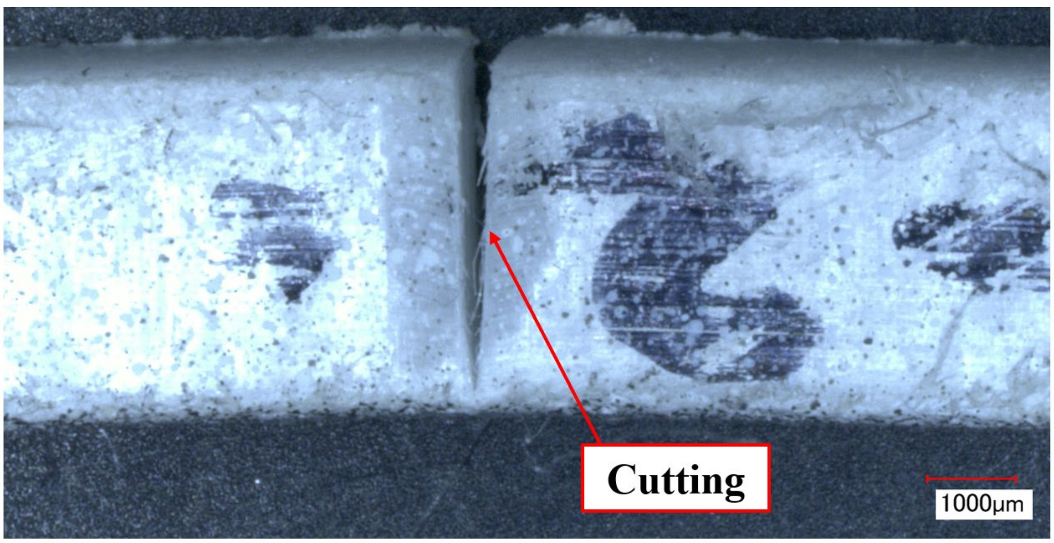

Figure 21. Example of cutting from low-rate indent experiment with razor indenter in backed configuration.

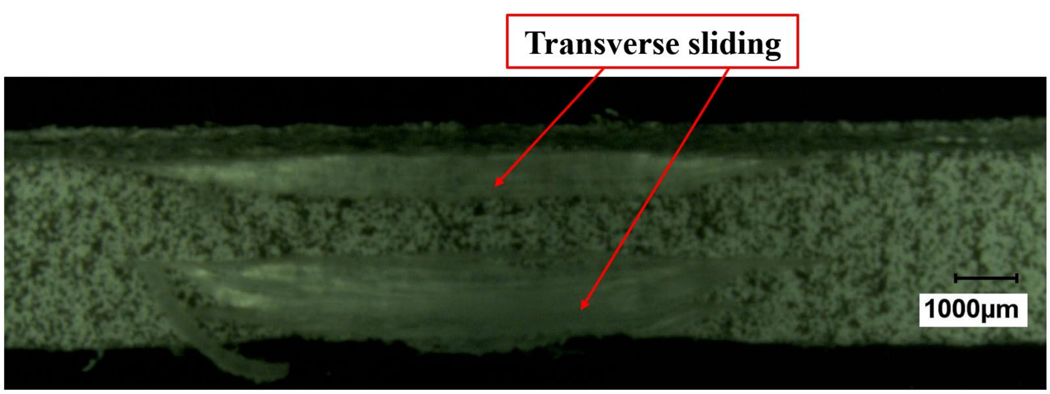

Figure 22. Example of transverse sliding from high-rate indent experiment with blunt indenter in backed configuration.

Table 2. Summary of deformation or failure modes for Tensylon 30A laminate indent loading experiments.

Configuration	Loading rate	Indenter	Deformation or failure mode observed
Backed	High	Blunt	Transverse sliding
		Inter	Pile-up, cutting
		Sharp	Pile-up, cutting
		Razor	Cutting
	Low	Blunt	Transverse sliding
		Inter	Pile-up, cutting, transverse sliding
		Sharp	Pile-up, delamination (large), transverse sliding
		Razor	Cutting
Unbacked	High	Blunt	Bending
		Inter	Bending, delamination (large)
		Sharp	Bending, delamination (large)
		Razor	Bending, delamination (small)
	Low	Blunt	Bending
		Inter	Bending, delamination (large)
		Sharp	Bending, delamination (large)
		Razor	Bending, delamination (large)

4. Discussion and Limitations

4.1 Spatial Averaging with DIC

Optical measurements of strain in specimens that contain strain gradients are sensitive to DIC analysis parameters, such as subset size and step size (Jones and Iadicola 2018; Thomas et al. 2025). Subset size dictates the area over which DIC performs spatial averaging; larger subset sizes produce strain data averaged over a larger area. This has the effect of decreasing the magnitude of strain in areas that have strain gradients if the subset size is not small enough (Gunnarsson et al. 2021). For the experiments documented here, the strain concentrations are highly localized and strain gradients large, so the strain data is likely dependent on the analysis parameters. This means that the strain magnitudes are likely larger at locations with large strain gradients than what has been measured.

4.2 Rate Limitations

The loading rates here are typical for material characterization in the dynamic SHPB regime; however, they may not be large enough to represent the material behavior during ballistic impact. The apparent stiffness and loads reported here for the high loading rate may not be representative of the laminate composite mechanical behavior during ballistic impact.

4.3 Experimental Repeatability

For most of the laminate indent experiments with indenter geometry and backing configurations discussed here, only one experiment was performed. However, for the solid backed intermediate geometry indenter at low loading rate, three experiments were performed. The first two (T36 and T38) both experienced transverse sliding with portions of the specimen not loaded by the indenter. This was solved by fabricating an indenter with a wider tip, which was used for the final experiment (T39). The experimental results are shown in Figure 23. The response is almost identical for all three, except the brief load drop region for the two experiments with the narrower tip where there is a small slip.

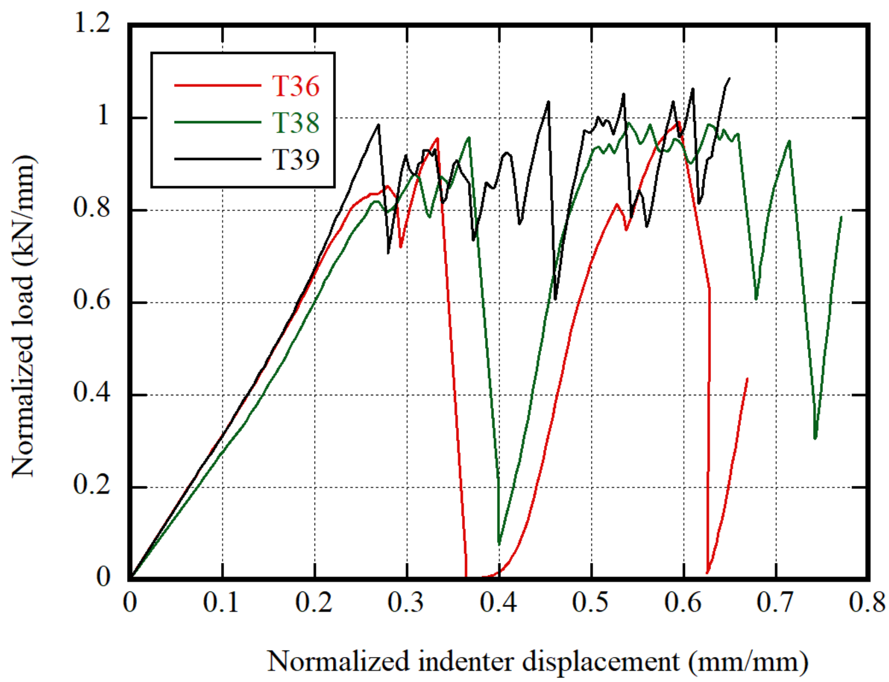

Figure 23. Normalized load vs. indenter displacement for Tensylon 30A laminate impact experiments in the backed configuration with intermediate geometry indenter at low loading rate.

4.4 Indenter Deformation

Indenters are assumed to be rigid in these experiments. Comparison of the indenter geometry pre- and postexperiment for blunt, intermediate, and sharp geometries indicated that minimal deformation occurred during loading. It was not possible to verify this assumption for the razor indenters as they fractured after cutting through the entire specimen and contacting the specimen backing at high rate. However, during loading with the razor indenter, the cutting/plateau load remained approximately constant, suggesting that the razor did not become blunted during loading.

5. Conclusions

An indent experimental method was developed to obtain the deformation and failure response of UHMWPE composites under different multiaxial stress states. The different stress states were selectively induced by changing as a function of three different variables: loading rate, indenter geometry, and loading configuration. The loading rates used were low and high rate, which were obtained using a modified SHPB. The indenter geometry was varied from ultra-sharp (razor blade) to blunt (half cylinder) to change the stress state in the TIZ and induce different dominant failure mechanisms.

Two different loading configurations were used to constrain the specimen: unbacked, in which the back of the specimen was free to deform during loading, and backed, in which the back of the specimen was constrained. The effect of these variables is summarized in Tables 1 and 2. The deformation and failure response were highly dependent on indenter geometry. Increasing the sharpness corresponded to lower magnitude load, as stress concentrated in the TIZ, and the failure mechanism changed from transverse sliding, induced by the blunt indenter, to shear cutting, induced with the razor blade. The effect of loading rate on the deformation response was marginal, with similar load response observed for both loading rates, with loading geometry held constant. Loading configuration had a large effect in the unbacked configuration, allowing the back surface to deform and causing the specimen to bend and delaminate. The unbacked configuration observed no shear cutting, pile-up, or transverse sliding mechanisms that were observed when the back surface was constrained, even when loaded by the razor indenter.

The utility of these experiments to the research community has been demonstrated. Prediction of failure during penetration of UHMWPE composites using computational frameworks that are based on rate-dependent subscale failure mechanisms requires the identification of thresholds for each dominant failure mechanism, which may also be a function of rate. Traditional depth-of-penetration experiments do not provide sufficient data for this. The 2D indent experimental techniques developed here are a distinct advantage by enabling measurements of full-field strain at the TIZ, which are not typically able to be obtained during traditional experiments. These strain fields within the specimen measured during the indentation process are critical for obtaining rate-dependent critical failure threshold parameters for failure modeling via inverse computational methods.

6. References

Alexander SL, Becker R, Weerasooriya T. An experimental-computational framework for UHMWPE films based on deformation and failure mechanisms: general approach and application to off-axis shear loading. DEVCOM Army Research Laboratory (US); 2023 Oct. Report No.: ARL-TR-9811.

Alexander SL, Weerasooriya T. Mechanical characterization of advanced ultra-high molecular weight polyethylene (UHMWPE) composites by ultrasonic method. DEVCOM Army Research Laboratory (US); 2021 Aug. Report No.: ARL-TR-9254.

Alexander SL, Weerasooriya T. A hybrid experimental-modeling-computational framework for UHMWPE based on deformation and failure mechanisms: extension to off-axis shear loading of fiber-based composites. DEVCOM Army Research Laboratory (US); 2024 June. Report No.: ARL-TR-9926.

Bogetti TA, Walter M, Staniszewski J, Cline J. Interlaminar shear characterization of ultra-high molecular weight polyethylene (UHMWPE) composite laminates. Compos Part A Appl Sci Manuf. 2017;98:105–15.

Chen WW, Song B. Split Hopkinson (Kolsky) bar: design, testing and applications. Springer; 2010 Nov.

Cline J, Love B. The effect of in-plane shear properties on the ballistic performance of polyethylene composites. Int J Impact Eng. 2020;143:103592.

Gunnarsson CA, Alexander SL, Weerasooriya T. Bending response of human skull as a function of loading rate and loading geometry. DEVCOM Army Research Laboratory (US); 2021 July. Report No.: ARL-TR-9215.

Gunnarsson CA, Alexander SL, Weerasooriya T. Tensile behavior of UHMWPE solid-state extrusion (SSE) film as a function of strain rate. DEVCOM Army Research Laboratory (US); 2022 Apr. Report No.: ARL-TR-9430.

Gunnarsson CA, Alexander SL, Weerasooriya T. Rate-dependent shear response during off-axis loading of fiber and film-based UHMWPE composites. DEVCOM Army Research Laboratory (US); 2023 Oct. Report No.: ARL-TR-9813.

Jones EMC, Iadicola MA, editors. A good practices guide for digital image correlation. International Digital Image Correlation Society; 2018.

Liu BG, Kandan K, Wadley HN, Deshpande VS. High strain rate compressive response of ultra-high molecular weight polyethylene fibre composites. Int J Plast. 2019;122:115–34.

Meshi I, Amarilio I, Benes D, Haj-Ali R. Delamination behavior of UHMWPE soft layered composites. Compos Part B Eng. 2016;98:166–75.

Reddy PR, Reddy TS, Srikanth I, Kushwaha J, Madhu V. Development of cost effective personnel armour through structural hybridization. Defence Tech. 2020;16(6):1089–97.

Sanborn B, DiLeonardi AM, Weerasooriya T. Tensile properties of Dyneema SK76 single fibers at multiple loading rates using a direct gripping method. JDBM. 2015;1(1):4–14.

Schreier H, Orteu JJ, Sutton MA. Image correlation for shape, motion and deformation measurements: basic concepts, theory and applications. Springer-Verlag; 2009.

Singletary J, Lauke B. Polyolefin film–reinforced composites for personal protection. Advanced Fibrous Composite Materials for Ballistic Protection. Woodhead Publishing; 2016 Jan 1. p. 389–408.

Thomas FD, Alexander SL, Weerasooriya T, Sockalingam S. Experimental investigation of the influence of dynamic multiaxial transverse loading on ultrahigh molecular weight polyethylene single fiber failure. Compos Part A Appl Sci Manuf. 2021;142:106250.

Thomas FD, Casem D, Weerasooriya T, Sockalingam S, Gillespie JW Jr. Influence of high strain rate transverse compression on the tensile strength of polyethylene ballistic single fibers. In: Dynamic Behavior of Materials, Volume 1: Proceedings of the 2018 Annual Conference on Experimental and Applied Mechanics; 2018 Oct 28. Cham: Springer International Publishing; p. 339–344.

Thomas FD, Sockalingam S, Sutton MA, Gunnarsson CA, Weerasooriya T, Alexander SL. High strain rate experimental characterization of mode II interlaminar shear response of UHMWPE film composites. DEVCOM Army Research Laboratory (US); 2025 May. Report No.: ARL-TR-10104.

List of Symbols, Abbreviations, and Acronyms

2D	Two-Dimensional
DIC	Digital Image Correlation
fps	Frames per Second
Inc	Incident
LED	Light-Emitting Diode
SHPB	Split-Hopkinson Pressure Bar
SSE	Solid-State Extrusion
TIZ	Target Interaction Zone
Trans	Transmission
TSL	Traction Separation Law
UD	Unidirectional
UHMWPE	Ultra-High-Molecular-Weight Polyethylene
VUMAT	Vectorized User Material

1 (PDF)	DEFENSE TECHNICAL INFORMATION CTR DTIC OCA
1 (PDF)	DEVCOM ARL FCDD RLB CI TECH LIB